Assessment of Pseudoshock Models Against Experiment in a Low-Aspect-Ratio Isolator

Louis M. Edelman* and Mirko Gamba†
University of Michigan, Ann Arbor, MI, 48109

Robin L. Hunt‡ and Aaron Auslender§
NASA Langley Research Center, Hampton, VA 23681

A highly confined shock train is investigated in a direct-connect isolator facility with a Mach 2 inflow and a constant-area low-aspect-ratio rectangular test section. High-speed schlieren imaging, wall static pressure measurements, surface oil-flow visualization, and particle image velocimetry from this isolator are synthesized into a three-dimensional schematic of the shock train structure. Against this, the prevailing pseudoshock models in the literature are assessed to evaluate the validity of their underlying assumptions. None of the prevailing pseudoshock models are found to simultaneously model the pressure and Mach number profiles, indicating a gap in the model formation and underlying assumptions when applied to the experimental isolator of interest. The presence of distortion in the isolator flowfield, such as a wall-bounded vortex, is found to skew the structure of the shock train, altering the strength and distribution of the compressive pressure gradient. It is further observed that the separated flow morphology surrounding the shock train is not monolithic, as is typically assumed, adjusting the balance of compressive forces within the shock cells. These findings lead to the conclusion that existing flux-conserved modeling approaches require modification to be effective in distorted and highly confined cases, including closure models that capture the three-dimensional distorted structure of the approach flow and its evolution along the shock train.

Presented as Paper 2022-0370 at the AIAA Scitech 2022 Forum
*Ph.D. Candidate, Dept. of Aerospace Engineering, AIAA Student Member, https://orcid.org/0000-0001-8862-7534
†Associate Professor, Dept. of Aerospace Engineering, AIAA Member
‡Research Aerospace Engineer, Hypersonic Airbreathing Propulsion Branch, AIAA Member
§Research Aerospace Engineer, Hypersonic Airbreathing Propulsion Branch, AIAA Member

Nomenclature

Variables

A	Duct Area
A_c	Integral Streamtube Area
A_{δ^*}	Displacement Area
A_θ	Momentum Deficit Area
a	Speed of Sound
C_f	Wall Friction Coefficient
D_h	Hydraulic Diameter
δ	Boundary Layer Thickness
Δt	Time Delay Between Laser Pulses
Δx	Streamwise Spatial Resolution
F	Stream Thrust
γ	Ratio of Specific Heats
H	Duct Height
$\dot{m}$	Mass Flow Rate
M	Mach Number
P	Pressure
Q	Waltrup-Billig Factor
R	Specific Gas Constant
Re_θ	Momentum Thickness Reynolds Number
ρ	Density
s_1	Leading Shock Stem Location
$s_2 - s_4$	Subsequent Shock Stem Location
s_f	Leading Shock Foot Location
σ	Pseudoshock Static Pressure Recovery Ratio
St	Strouhal Number
T	Temperature
θ	Momentum Thickness
u	Streamwise Velocity
W	Duct Width
$y+$	Non-Dimensional Wall Distance
x	Streamwise Axis
y	Lateral Axis
z	Vertical Axis
$\overline{X}$	Average of Variable X
$\tilde{X}$	Uncertainty of Variable X

Subscripts

0	Approach Condition Value
1	Flux-Conserved Value
2	Post Pseudoshock Value
A	Isolator Entrance Value
B	Isolator Exit Value
i	i^{th} Sample or Frame

I. Introduction

The dual-mode scramjet (DMSJ), shown schematically in Figure 1, is a high-speed airbreathing engine. It operates as a ramjet at lower freestream Mach numbers ($3 \sim 5$) with mostly subsonic flow in the combustor and as a scramjet at higher freestream Mach numbers ($M \geq 5$) with mostly supersonic flow in the combustor. Between the inlet and

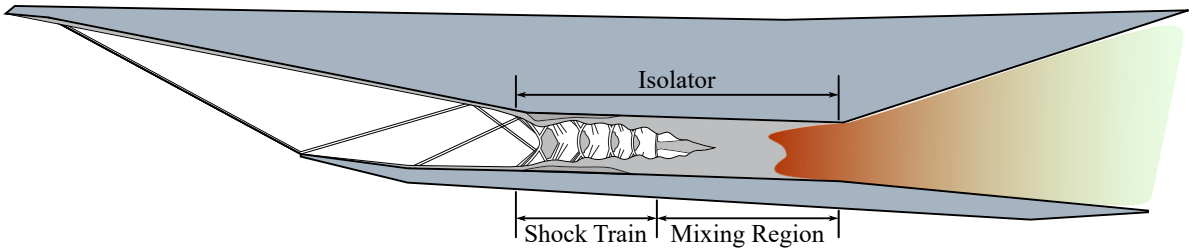

Fig. 1 Schematic of a normal bifurcated shock train in a DMSJ engine.

combustor sits the isolator, a constant or nearly constant area duct. As the engine transitions between ram and scram modes, the isolator contains the pseudoshock, a complex compressive flow structure that forms as a result of backpressure in the combustor.

Matsuo et al. [1] provide a comprehensive survey of steady-state pseudoshock behavior with a more contemporary survey performed by Gnani et al. [2] to include some discussion of passive control. The pseudoshock is typically divided into two streamwise regions. Upstream is the shock train, a mostly supersonic region dominated by a series of interconnected shock-boundary layer interactions (SBLIs) separated by re-expansion regions called shock cells. The downstream region, or mixing region, is instead a shock-free, lower Mach number region dominated by turbulent flow. Two types of shock trains can manifest in a DMSJ: a normal bifurcated shock train, typically at lower freestream Mach numbers, or an oblique shock train, typically present at higher freestream Mach numbers [3]. Downstream of the shock train is the mixing region where mixed sub/supersonic flow yields further compression. At lower freestream Mach numbers, the shock train position in the isolator is highly sensitive to the combustor backpressure, adjusting the relative lengths of the shock train and mixing region within the pseudoshock [4]. This study focuses on the normal bifurcated shock train to understand the dynamical structures and mechanisms critical to operating in this regime, which a DMSJ must pass to achieve high Mach, hypersonic flight.

Complicating matters, the shock train exhibits inherent unsteadiness, whereby the shock train erratically shifts in the streamwise direction about a time averaged position, despite relatively constant inflow and backpressure conditions. The spectral quality of the inherent unsteadiness was studied by Sugiyama et al. [5] and expanded upon by Hunt and Gamba [6] to detail the origin of unsteadiness within the pseudoshock. To make analysis more tractable, the shock train is treated as a time averaged, quasi-steady structure. The location and properties of a quasi-steady shock train are controlled by the development of isolator Mach number and boundary layer properties balanced against the backpressure of the downstream combustor. A central area of research is the structure and dominant flow physics of the shock train structure between these controlling boundary conditions.

The shock train structure is typically represented as a two-dimensional structure, derived from schlieren imaging, or a quasi-1D pressure profile along the streamwise length of the isolator, derived from wall static pressure taps. While quantitative and qualitative data can be gleaned from schlieren, it is a line-integrated technique that only resolves a

two-dimensional representation of the complex SBLI structures. Wall static pressure measurements are used extensively for understanding the time averaged profile of the shock train, however the smearing effect of thick boundary layers and limited spatial resolution abstracts these measurements from the shock structures and filters unsteadiness. These techniques obfuscate unsteady behavior and collapse down the importance of three-dimensional effects such as corner flows in rectangular ducts and boundary layer confinement [7, 8].

Carroll and Dutton [8] investigated these three-dimensional effects on oblique (isolator inflow $M = 2.45$) and normal bifurcated (isolator inflow $M = 1.6$) shocks trains in a symmetric rectangular duct using schlieren imaging, surface oil flow visualization, and laser Doppler velocimetry. While large corner separation bubbles were observed in the oblique case, only small incipient separation bubbles were observed below the first shock in the bifurcated case. More recently, Morgan et al. [9] performed large-eddy simulations (LES) to match the bifurcated case and observed a strong dependence between boundary layer confinement and the shock structure. They concluded that spanwise confinement, and thus corner effects, must be included to successfully model shock train behavior. This was further corroborated by Fiévet et al. [10] for a shock train with Mach 2 isolator inflow. Using a direct-connect isolator with a Mach 2.5 inflow, Geerts and Yu [11] observed a shock train with shadowgraph from two orthogonal fields-of-view to elucidate the effect of path-integration on rendering the shock train. They found that the shock structures are highly three-dimensional with the structure initialized and controlled by corner separation, even in a high aspect ratio duct.

These findings are consistent with the results of Hunt and Gamba [6, 12] in a low aspect ratio model isolator. They made detailed observations of the leading SBLI structure from schlieren imaging and cross-sectional stereoscopic particle image velocimetry (SPIV) below the leading lambda foot. These observations demonstrate the importance of separated corners in the generation and propagation of unsteadiness within a highly confined shock train. Furthermore, they found that the leading SBLI structure becomes more oblique, and thus corner dominated, the farther upstream the shock train sat in the isolator. This corresponds primarily to changes in the boundary layer ingested by the shock train.

A key area of shock train research in the historical and contemporary literature is to collapse the complex, unsteady structure down to a computationally tractable quasi-1D model for fast design optimization and online control of DMSJ engines [1, 13–17]. In pursuit of this research objective, this study analyzes the relevance and validity of the assumptions underpinning correlative and flux-conserved shock train modeling methodologies by comparing the model predictions against experimental measurements in a Mach 2 direct-connect isolator facility. These measurements include high-speed schlieren imaging [18], streamwise particle image velocimetry planes, wall static pressure traces [4], and surface oil flow visualization [6]. The measurements are synthesized to infer a detailed three-dimensional representation of the shock train to include the sonic surface bounding the core flow, the shock structures, and the separation bubbles. The following analysis focuses on the importance of complex flow structure interactions and asymmetry in the isolator flow field that drive shock train structure, including the ability of prevailing models to predict the fluid dynamical state of the average flow properties streamwise along the shock train.

II. Shock Train Modeling and Key Assumptions

A. Classical Models

The earliest proposed pseudoshock or shock train reduced-order models collapse the system down to a tractable, quasi-1D jump conditions. These models take in a set of approach conditions, which are the average freestream and boundary-layer properties entering the shock train, and output estimates of the pseudoshock length and pressure rise. For example, McLafferty [19] proposed flux-conserved averaging or stream thrust averaging. The mass, momentum, and continuity equations are integrated over an imaginary control volume between stations 0 and 1, as shown in Figure 2, to conservatively convert a velocity profile with centerline values of M_0, P_0, and T_0 into a quasi-1D, uniform profile with values M_1, P_1, and T_1 [19] with equivalent blockage and momentum deficit.

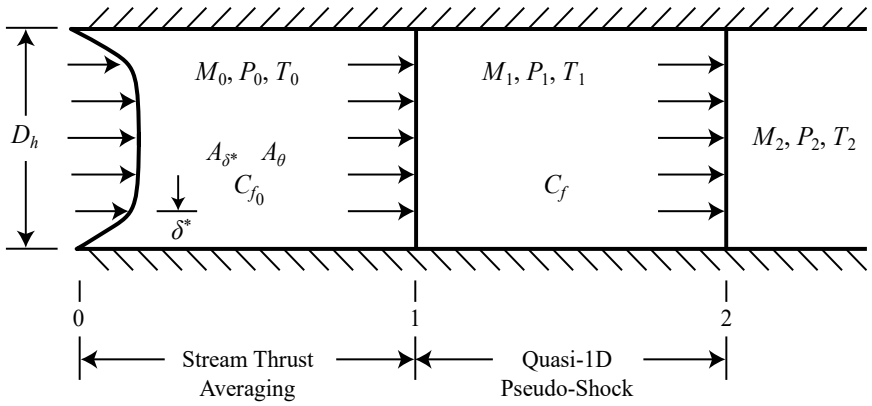

Fig. 2 Diagram of McLafferty's [19] flux-conserved stream thrust averaging procedure to estimate approach conditions (stations 0-1) and compute pressure jump conditions across the pseudoshock (stations 1-2).

The flux-conserved, quasi-1D approach conditions are integrated over the cross-section of the duct A_c with a known displacement thickness blockage, A_{δ^*}, and momentum thickness blockage, A_θ, as defined in Equations 1–6 [19]. The value u is the streamwise velocity, ρ is the density, and a is the speed of sound, all evaluated as a function of streamwise position x. R is the specific gas constant, γ is the ratio of specific heats, $\dot{m}$ is the mass flow rate, and T_t is the total temperature, which are taken to be constant along the pseudoshock.

$$F = \iint_{A_c} P \mathrm{d}A + \iint_{A_c} \rho u^2 \mathrm{d}A = P_0[A + \gamma M_0^2 (A - A_{\delta^*} - A_\theta)] \tag{1}$$

$$\dot{m} = \iint_{A_c} \rho u \mathrm{d}A = P_0 M_0 \sqrt{\frac{\gamma}{RT_0}} (A - A_{\delta^*}) \tag{2}$$

$$u_1 = \frac{\gamma}{\gamma+1}\frac{F}{\dot{m}} + \sqrt{\left(\frac{\gamma}{\gamma+1}\frac{F}{\dot{m}}\right)^2 - \frac{2\gamma R T_t}{\gamma+1}} \tag{3}$$

$$a_1 = \sqrt{\gamma R \left[T_t - \frac{u_1^2}{2R}\left(1 - \frac{1}{\gamma}\right)\right]} \tag{4}$$

$$M_1 = \frac{u_1}{a_1} \tag{5}$$

$$P_1 = \frac{F}{A} - \frac{\dot{m}u_1}{A} \tag{6}$$

While computationally tractable, the flux-conserved averaging approach brings with it fundamental assumptions that abstract the complexity of incoming flow and washes-out distortion. It is thus assumed that in-plane flow velocities are negligible such that there are no large fluid dynamical structures, such as vortices, in the isolator inflow.

McLafferty [19] modeled the pseudoshock pressure rise as a normal shock jump between the quasi-1D flux-conserved conditions from station 1 to 2 in Figure 2 with frictional momentum loss defined by Δ. The key assumption underlying this approach is that the pseudoshock behaves as an extended normal shock with an estimated total pressure loss. The primary output of this model is σ, the fraction of static pressure recovered in comparison to an inviscid duct with uniform flow across a normal shock evaluated at M_0 [19].

While the overall pseudoshock pressure jump computed by McLafferty [19] and similar methods [20, 21] is useful for initial DMSJ engine designs, the full, streamwise pressure profile along the isolator is of greater interest as it drives the isolator length and is relatively easy to measure for control purposes. One of the earliest pressure profile models is Crocco's shockless model [22]. Crocco treats the pseudoshock as a series of oblique shocks in a supersonic core surrounded by a highly turbulent boundary layer that consumes the core via turbulent dissipation. Given that for the same amount of compression, a series of oblique shocks will produce much less entropy than a single normal shock, Crocco assumes the core flow is isentropic with compression transferred to the wall static pressure by turbulent dissipation in a surrounding boundary layer. Due to the low subsonic nature of the boundary layer, it is further assumed that wall friction forces are negligible.

As with McLafferty [19], Crocco initializes the shockless model as a flux-conserved uniform flow, adopting the same quasi-1D assumptions described previously. The conservative flow equations are integrated streamwise in two uniform regions, a dissipative boundary layer and an inviscid core. The pressure is assumed to be equal over the duct cross-section with equal pressures in each region. The pressure profile is the primary output of the model with the pseudoshock length defined as the point where the dissipative boundary layer fully consumes the inviscid core. While computationally efficient, the nature of the inviscid assumption lends this method only to high Mach number, fully oblique pseudoshocks with relatively low and constant pressure gradients [1].

A conceptually simple alternative to these theoretical models are empirically derived correlations, chief among them the Waltrup-Billig Correlation developed for cylindrical isolators [13] and later rectangular isolators [14]. The correlation for rectangular ducts is defined in Equation 7 where H, M_0, P_0, θ, and Re_θ are the isolator duct height, centerline Mach number, static pressure, wall momentum thickness, and momentum thickness Reynolds number, respectively, at approach conditions just upstream of the pseudoshock.

$$50\left(\frac{P}{P_0}-1\right)+170\left(\frac{P}{P_0}-1\right)^2=\frac{x(M_0^2-1)Re_\theta^{1/5}}{\sqrt{H\theta}} \tag{7}$$

Sullins and McLafferty [7] later applied the inflow flux-conserved conversion as a modification to the Waltrup-Billig correlation [13]. This work experimentally verified the key approach conditions that control the scaling and structure of the pseudoshock [4] and informed the development of the contemporary class of correlation driven, streamtube integrated models known as integral flux-conserved models.

B. Contemporary Flux-Conserved Models

The contemporary flux-conserved modeling approach, originated by Smart [15], is an evolution of Crocco's shockless model. Both consider a supersonic core flow surrounded by a low-speed, subsonic turbulent boundary layer. Smart treats the pseudoshock as a quasi-1D streamtube bounded by a fully separated displacement area, A_{δ^*}, such that there is no wall friction ($C_f = 0$). Furthermore, all mass flow is assumed to pass through a core region, $A_c = 1 - A_{\delta^*}$. The flux-conserved model integration solves simultaneously for the streamtube to duct area ratio, A_c/A, and Mach number, M^2, and predicts a monotonically increasing pressure profile. The initial integration values are again seeded by the McLafferty [19] flux-conserved approach conditions, carrying with them the key assumptions of negligible in-plane flow, uniform in-plane pressure, and the lack of large-scale fluid structures in the isolator.

The key departure from Crocco's model is the inclusion of a closure model to impose the compressive effect of the shock train system on the integration by the single parameter Ortwerth diffusion model [23]. The Ortwerth model parameter, k, to the local quasi-1-D dynamic pressure and the wall friction coefficient evaluated at the approach condition of the shock train. This relies on the assumption, similarly to Crocco, that compression sustained by the shock train is transferred to and limited by the diffusion to the wall in the boundary layer.

Fiévet et al. [17] expanded the flux-conserved approach by replacing the single parameter Ortwerth closure model with a nine parameters representation to add flexibility. These account for nonuniform kinetic energy transfer along the pseudoshock, allow for nonzero wall friction, and add scaling by the McLafferty predicted pressure recovery, σ. The power of flux-conserved modeling stems from the ability of the physics-based integration to scale with relevant approach conditions in a computationally tractable manor. Because of this, flux-conserved modeling approaches are attractive tools for engine design and fluid dynamical research. As such, this study focuses on assessing the validity of the flux-conserved model assumptions and rendered flow physics against a suite of experimental measurements.

A summary of the assumptions underlying the above shock train modeling approaches are summarized in Table 1. Contextualized by the intended use of these literature models, this study assesses each assumption against data and observations generated in the facility used for this study.

Table 1 Summary of assumptions relevant to prevalent quasi-1D pseudoshock models in the literature. ✓ indicates assumption made in model, × indicates assumption not made in model.

	Assumption	Waltrup Billig [14]	McLafferty Jump [19]	Crocco Shockless [22]	Smart Flux-Conserved [15]	Fiévet Flux-Conserved [17]
1.	Empirically Calibrated	✓	×	×	×	×
2.	No Transverse Momentum Flux Accounting	×	✓	✓	✓	✓
3.	Negligible Transverse Flow (Quasi-1D)	×	✓	✓	✓	✓
4.	Undistorted Shock Train Structure	×	✓	✓	✓	✓
5.	Uniform Transverse Pressure	×	✓	✓	✓	✓
6.	Monolithic, Symmetrical Separated Boundary Layer	×	×	✓	✓	✓
7.	Zero Wall Friction ($C_f = 0$)	×	×	✓	×	×
8.	Isentropic Core	×	×	✓	×	×
9.	Only Mass Flow Through the Core	×	×	×	✓	✓
10.	Compression Due to Dissipation Only Within the Turbulent Boundary Layer	×	✓	✓	×	×
11.	Compression Due to Exchange of Kinetic and Thermal Energy in the Core	×	×	×	✓	✓
12.	Constant Total Temperature	×	✓	✓	×	×
13.	Characteristic Length Scale	H	D_h	D_h	D_h	D_h
14.	Calibrated Mach Range, M_0	$1.5 - 2.7$	N/A	N/A	$1.8 - 3.7$	$1.3 - 2.8$

III. Experimental Facilities and Measurements

A. Direct-Connect Isolator Facility

The experimental facility, diagrammed in Figure 3, is a supersonic wind tunnel that draws atmospheric air through an asymmetric, two-dimensional Mach 2 nozzle into a constant-area rectangular test section with a duct height, H, of 69.8 mm and a height-to-width aspect ratio of 1.2. The coordinate system is fixed at the nozzle throat with positive x in the streamwise direction. The test section side walls and a reconfigurable bottom wall plug, shown by the hashed region in Figure 3, can be swapped between pressure transducer instrumented and borosilicate glass window versions. While the side windows provide full optical access, the bottom panel window is only able to provide access to the middle 70% of the test section for a streamwise extent of 6.5H. Following the test section, a diffuser connects the tunnel to a butterfly

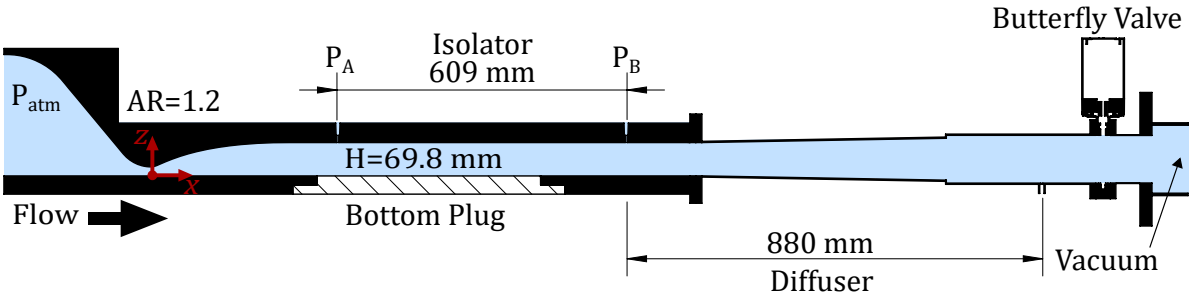

Fig. 3 Diagram of the experimental facility.

valve that mechanically chokes the flow venting into a vacuum chamber.

The pressure ratio across the test section, P_B/P_A, is measured by a pair of absolute capacitance manometers along the top wall. For this study, the normal bifurcated shock train in the facility has an isolator pressure ratio of $2.8 \sim 3.2$ and a typical static pressure recovery ratio, σ, of 0.72 as defined by the percentage of static pressure recovery across a normal shock with the same inflow Mach number.

B. Time-Resolved Schlieren Imaging

The shock structure is visualized by a Z-type schlieren system that qualitatively resolves the density gradient field along the streamwise x-direction of the test section. Illumination is provided by a continuous white LED and a high-speed camera captures the frames at 10 kHz with a 2 μs exposure. An example of an instantaneous schlieren frame is shown in Figure 4. The streamwise location of the leading shock Mach stem, s_1, is quantified by scanning pixel intensity along $z/H = 0.6$ at the center of the stem. The subsequent shock features, $s_2 - s_4$, are detected along the same line-scan. Spatial uncertainty due to the pixel pitch of the camera, the resolution of each pixel, and averaging over the 2 μs exposure is approximated to be $0.014H$ for these features. The leading shock foot location, s_f, is selected visually from the average schlieren frame to approximate where the leading lambda foot contacts the boundary layer on the bottom wall.

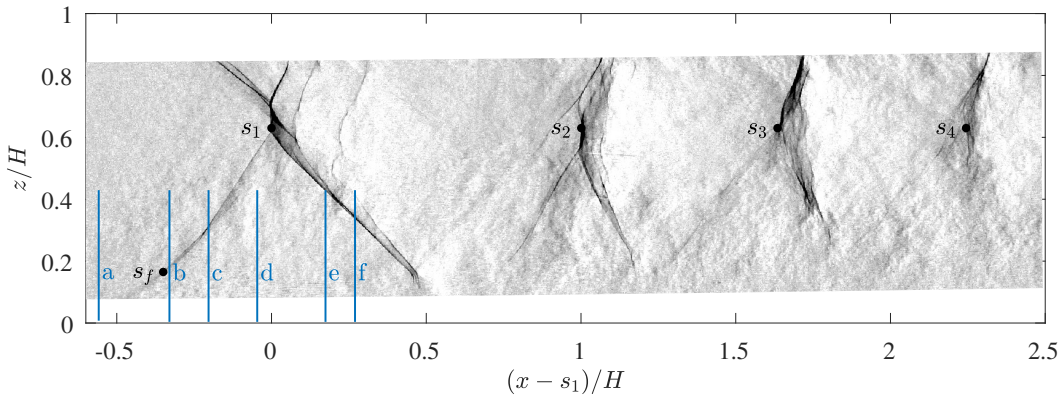

Fig. 4 Instantaneous schlieren frame with labeled shock features and y-locations of cross-sectional SPIV planes a-f.

To resolve the structure of the shock train independent of the inherent unsteadiness, the x-coordinate is shifted for each schlieren frame such that $s_1 = 0$, which is referred to as the stem-aligned reference frame. Overlapping all schlieren images onto the same grid yields an uncertainty on the order of the grid resolution, $\pm\Delta x$. Combined with the uncertainty in the shock stem locations, this yields RMS uncertainties of $0.0142H$.

C. Oil Flow Visualization

Surface oil flow visualization on the side and bottom walls resolves the time-averaged boundary layer structure. A thin base coat of 100 cSt silicone oil is seeded with a titanium dioxide-oil mixture. After tunnel startup, the valve is set to position a shock train in the test section and flow pattern development is observed. The procedure is repeated first with cameras focused on the side and bottom walls, and then with both cameras aligned streamwise on the side wall. A composite average of the flow structure in the corner is shown in Figure 5. To bring these oil flow images into the stem-aligned reference frame, the leading edge of the side wall SBLI is set to approximately the same streamwise location as the shock foot, s_f, in the schlieren imaging.

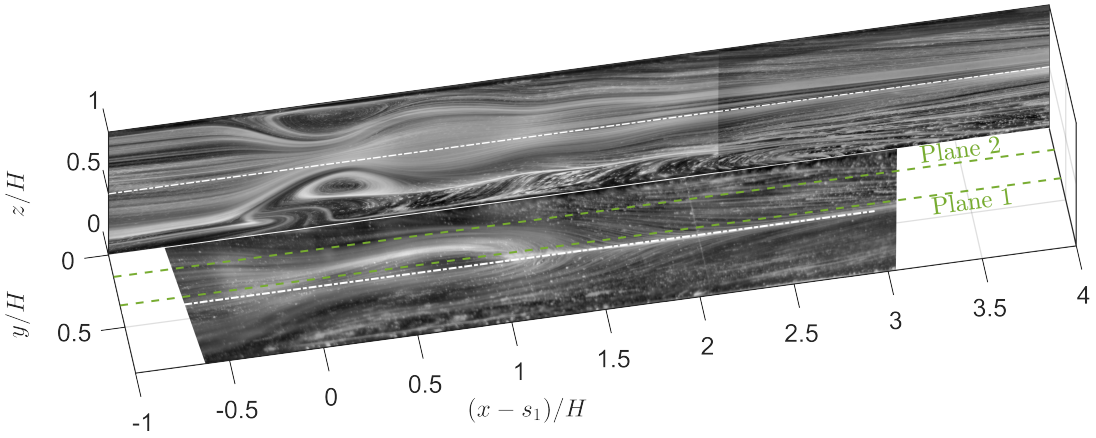

Fig. 5 Oil flow visualization with flow from left to right. Green lines show the location of streamwise PIV planes. Pressure ports are located along the white lines.

D. Time-Averaged Wall Pressure Measurements

Time averaged, streamwise pressure measurements are sampled at 100 Hz through 0.8 mm diameter pressure taps along the side and bottom wall centerlines as marked on Figure 5 with a varying spacing of 12.7 mm or 25.4 mm. The taps are connected via flexible tubing to three ±17.2 kPa and one ±103 kPa differential pressure scanners for a total of 63 channels. All scanner measurements are referenced to the upstream static pressure tap on the top wall of the isolator, P_A. The root-mean-square (RMS) uncertainty in the pressure scanner measurements are ±30 Pa and ±60 Pa for the low and high range pressure scanners, respectively. The higher range scanner channels are restricted to the most downstream pressure taps where the relative pressure differential is high, and thus, the higher uncertainty is less impactful.

The leading shock foot location, s_f, where the shock contacts the boundary layer, is estimated using the bottom wall

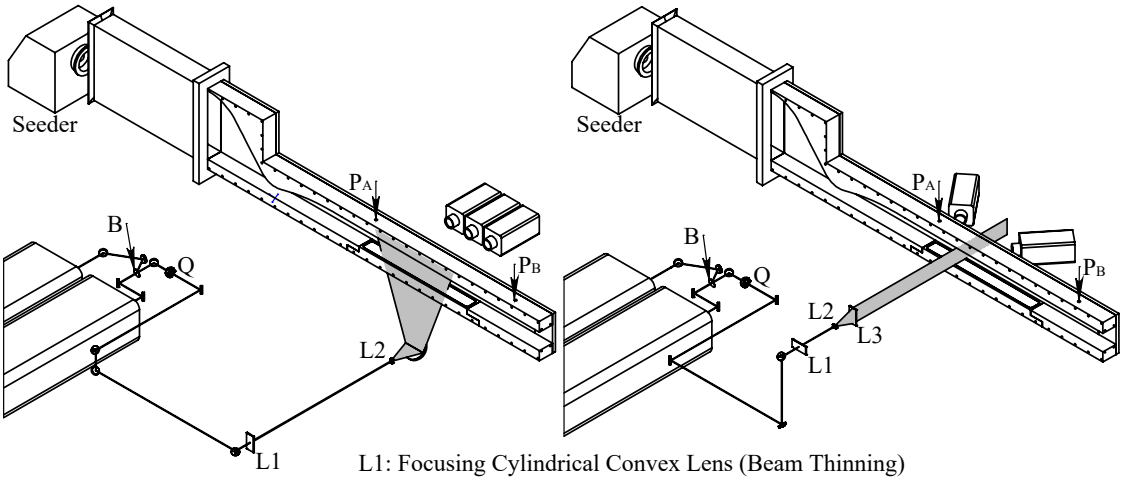

Fig. 6 Diagram of the streamwise PIV (left) and the cross-sectional SPIV (right) configurations.

pressure traces by finding the first peak in the streamwise pressure variance gradient $\mathrm{d}\sigma(P)^2/\mathrm{d}x$ [4]. All of the wall static pressure data is shifted to the stem-aligned reference frame (with $s_1 = 0$) by matching this s_f to that of the average schlieren imagery, as shown in Figure 4.

E. Particle Image Velocimetry

Two sets of particle image velocimetry (PIV) data are included in this study: streamwise two-component planes and stereoscopic PIV (SPIV) cross-sectional slices. The streamwise PIV renders the streamwise, u, and vertical, w, velocity fields in the $x-z$ plane while the SPIV measurements resolve all three velocity components in $y-z$ planes.

A Laskin nozzle generator seeds the facility inlet with ~ 0.7 μm diameter, 819 kg/m^3 density polyalphaolefin oil particles with a Stokes number of St $\approx 5\times10^{-6}$. The particles are distributed to an array of injection ports and diffused throughout the field-of-view by a mixing fan in the inlet. Based on the particle relaxation distance across the normal shock stem at s_1, the worst-case uncertainty in PIV derived shock locations is approximately $0.03H$. This is sufficiently low to track the large-scale motions of the shock structures in a compressible flow with some particle tracking error to be expected in large gradient areas such as shocks [24].

Both cases are processed by four passes of 32×32 Gaussian-weighted windows with a 75% overlap to yield vector field resolutions of 0.63 mm and 0.27 mm for the streamwise and cross-sectional cases, respectively. PIV vectors with a correlation peak less than 1.1 are removed and Grubbs' test for outliers is applied at each grid point to eliminate spurious samples. The Mach number, M, field is computed assuming constant total temperature such that the local flow speed is directly related to the local temperature and thus Mach number by the adiabatic flow relations [25].

In the streamwise case, measurements are taken for two planes: $y = 0.44W$ (i.e., close to the test section centerline) and $y = 0.20W$ (i.e., close to the test section sidewall) referred to as Plane 1 and Plane 2, respectively. The streamwise extent of the streamwise planes is limited to $4H$ by the practical geometry of beam forming optics shown in Figure 6. As with the other measurement types, the streamwise PIV frames are shifted to the stem-aligned reference frame (with $s_1 = 0$) to resolve the structure of the shock train independent of the inherent unsteadiness. The shock stem is located in each frame of the PIV data and then shifted to overlap all frames on the same grid yielding an uncertainty on the order of the grid resolution, $\pm\Delta x$. The same procedure is applied to the normal shock stem for both Plane 1 and 2. Combined with the uncertainty in the shock stem locations, this yields an RMS uncertainty of $0.0313H$ for the PIV alignment.

In the cross-sectional case, the laser sheet is raised to the level of the isolator through a combination of optics to illuminate a spanwise plane at $x = 7.22H$, about which the shock train oscillates due to the inherent unsteadiness. Measurements with no shock train in the isolator are averaged to generate an approach condition plane referred to as Plane a. Backpressured instances are located relative to s_1 and sorted into 5 bins of 160 samples each by approximately matching the trend in centerline displacement thicknesses between streamwise Plane 1 and each cross-sectional frame. The streamwise location of each cross-sectional SPIV Plane a-f, relative to s_1, is shown in Figure 4.

Velocity uncertainties in each frame are computed for each velocity component by the correlation statistics method of Wieneke [26]. Applied using DaVis 8.4, the asymmetry of the correlation function within each interrogation window is related to uncertainty in the computed displacement vector and thus the computed velocity components. This validated methodology [27, 28] accounts for sources of error including random particle motion, out-of-plane motion, camera noise, and shadowgraph effects. The uncertainty of each i-th frame, $\tilde{u}_i$, is then cascaded into the average velocity, $\overline{u}$, and average Mach number, $\overline{M}$, fields via RMS uncertainty propagation at each grid point, represented by $\tilde{u}$ and $\tilde{M}$, respectively. The PIV-derived velocity uncertainty for each vector in each frame, u_i, increases as seed particles accumulate in the shocks and separation bubbles [24]. Unsteadiness, such as within separated flow regions, further increases uncertainty in the average profiles. For example, the Mach number uncertainty ranges from ± 0.04 at the leading shock stem to ± 0.14 at the end of the Plane 1 field-of-view.

Figure 7 shows the aligned streamwise measurements: time averaged schlieren, streamwise PIV, and wall static pressure, and PIV profile averaged Mach number to highlight the correlation between the measurement techniques.

IV. Three-Dimensional Schematic of the Facility Shock Train Structure

The suite of measurements aligned and shown in Figure 7 each provide a different and valuable perspective on the structure of the isolator shock train. Leveraging this collection of datasets, this study constructs a three-dimensional representation of the low aspect ratio Mach 2 isolator shock train of interest. This will then be applied as a tool to assess the limitations of the assumptions underpinning the current state-of-the-art pseudoshock models summarized in Figure 1.

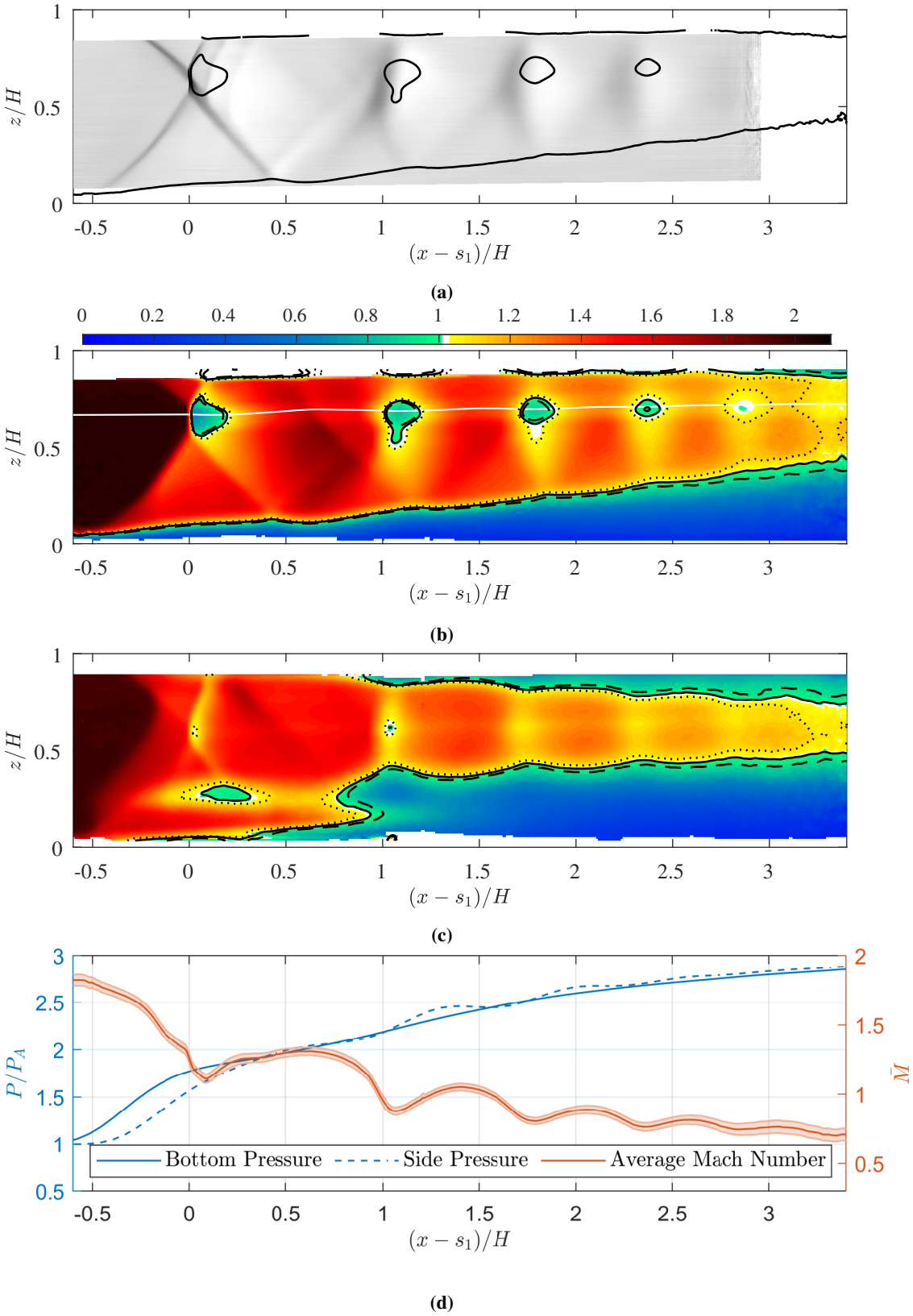

Fig. 7 Examples of stem-aligned data a) time-averaged schlieren image, b-c) Time-averaged Mach contours of PIV Plane 1-2, and d) Wall pressure (blue) and 1D profile averaged PIV Mach number (red). $\overline{M} = 1$ **(solid black line in a-c),** $\overline{M} - \widetilde{M} = 1$ **and** $\overline{M} + \widetilde{M} = 1$ **(dotted and dashed lines, respectively, in b-c), and streamline through the strong center of each SBLI (white line in b).**

To start constructing a 3D image of the shock train, regions of probable reverse, or separated, flow are considered. These regions are estimated by assessing the fraction of SPIV frames with instantaneous reverse velocities, $u_i \leq 0$. A region with greater than 50% reversed frames is considered to be region of probable separation. Figure 8 shows averaged PIV images of the cross-sectional Planes a–f. The black dashed lines on each plot indicates the region of reverse flow within the conservative limit of $u_i \leq \tilde{u}_i$ where $\tilde{u}_i$ is the instantaneous uncertainty of each vector. The black solid line represents the average sonic line at $\bar{M} = 1$. White streamlines are included for Plane a in Figure 8a to highlight the presence of a vortex upstream of the shock train. The impact and importance of this vortex is analyzed in more detail later.

Figure 9 shows contours of the reverse flow probability for the streamwise PIV planes. These illustrate that no point within the resolved field-of-view has greater than 50% reversed flow. This suggests that a stable separated flow region as prominent as the corner separation observed by the oil-flow visualization in Figure 5 and the cross-sectional PIV in Figure 8 does not extend into the measured field-of-view in Plane 1 or 2. Instead, a threshold of at least 10% reversed flow is considered to indicate the presence of intermittent separation significant enough to influence the average flow structure. To account for measurement uncertainty, the dashed and dotted lines in Figure 9 correspond to 10% probability of $|u_i| \leq \tilde{u}_i$.

The regions of strong, separated flow are shown as numbered green bubbles in Figure 10. The top corner separated regions, numbered 1 and 2, are extracted from the oil flow visualization in Figure 5. The strongest corner separation region, 3, is extracted from the oil flow visualization in Figure 5 and the corner SPIV in Figure 8. The oil flow visualization in Figure 5 and streamwise PIV reverse flow contours in Figure 9 imply the presence of weak and intermittent separated regions noted as 4, 5, and 6 in Figure 10. Additional, top wall separations may be present but are not observed due to the bias of available data toward the more complex bottom corner regions. However, since separated regions 4-6 are weak and intermittent, the presence of significant separations on the top wall is unlikely due to the stronger boundary layer attachment on that surface. The cause of this asymmetry and the influence of the separated flow morphology on the core structure are discussed in the following sections.

Next the sonic surface, shown as a translucent blue envelope in Figure 10, is constructed from the streamwise and cross-sectional PIV measurements. The average streamwise PIV sonic lines from Figure 7b-c are intersected with the sonic lines in the cross-sectional SPIV in Figure 8. Lateral symmetry is inferred from the oil flow rendered separation bubble symmetry at $-0.5 \leq x/H \leq 1.5$ in Figure 5. Due to laser reflections from the test section walls, information on the top wall boundary layer is limited. Extrapolation from the unbackpressured computational fluid dynamics (CFD) and the side wall oil-flow visualization is used to infer the upper edge of the sonic surface. High uncertainty in the PIV-derived sonic line forces downstream closure of the sonic surface to be estimated in the $3.2 \leq x/H \leq 5$ range with the average profile used to estimate closure at $\sim 4H$. The shape of this closure is inferred from the convergence of oil-flow streamlines and the morphology of the streamwise PIV sonic line uncertainty bounds.

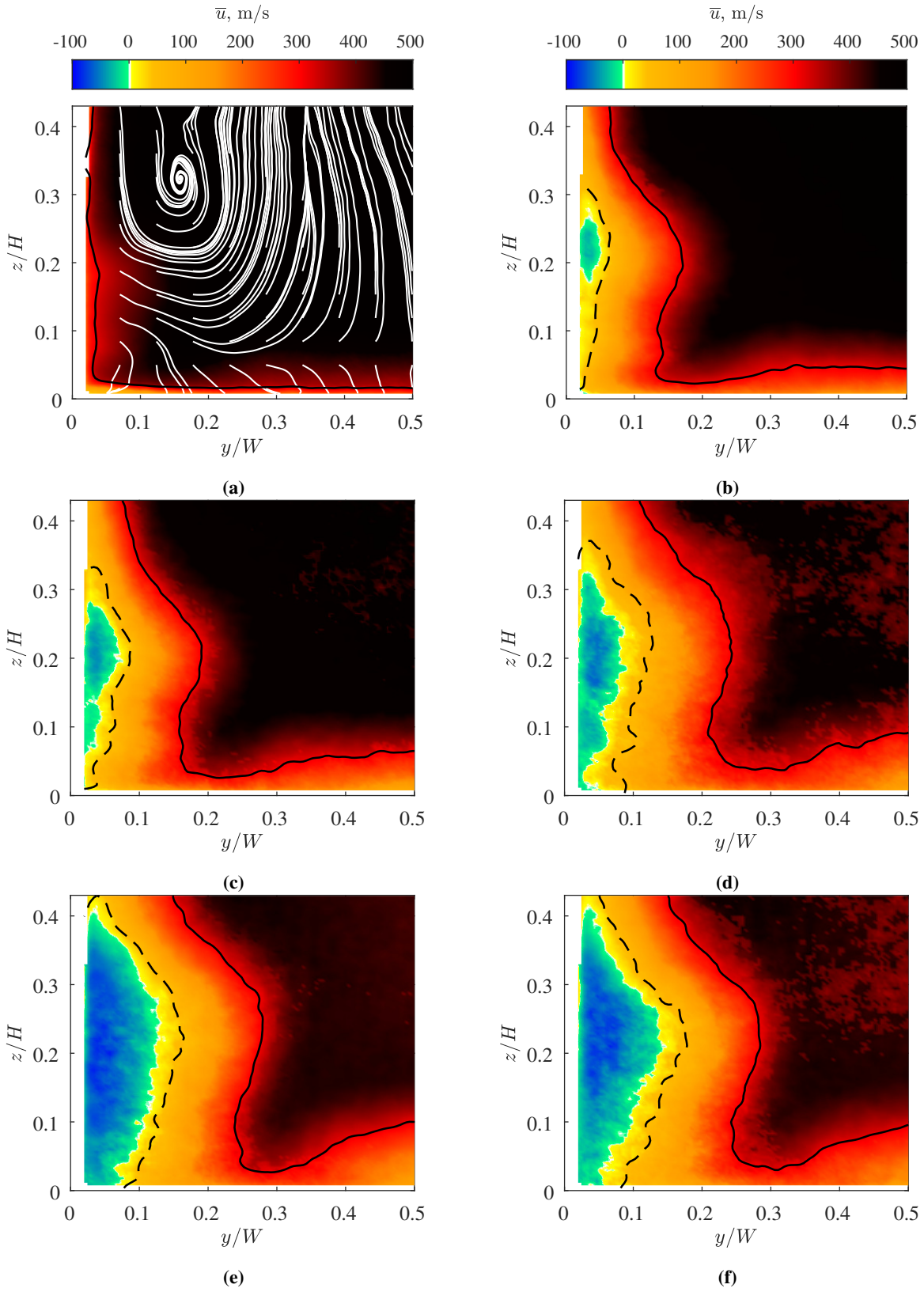

Fig. 8 Average streamwise velocity contours of cross-sectional PIV Planes a-f defined in Figure 4. White lines: in-plane streamlines. Dashed black line: 50% region of probable reverse flow. Solid black line: $\overline{M} = 1$.

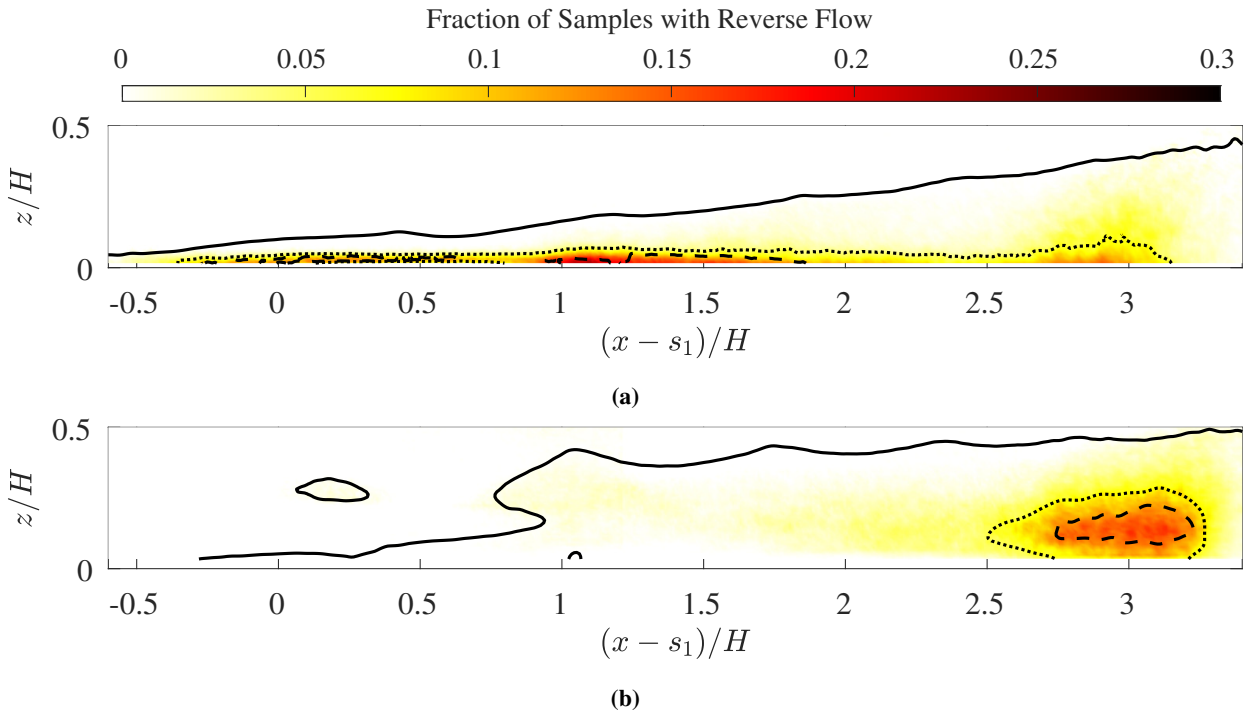

Fig. 9 Fraction of PIV frames with reverse flow: (a) Plane 1 (near centerline); (b) Plane 2 (near side wall). Overlaid lines represent: $\overline{M} = 1$ (solid line), 10% $u_i \leq -\tilde{u}_i$ (dashed line), and 10% $u_i \leq \tilde{u}_i$ (dotted line).

Next, the series of shocks comprising the shock train are modeled. The centerline shock profiles for the first four structures are extracted from the instantaneous and average schlieren images in Figures 4 and 7a, respectively. Two additional shock structures are evident from the Plane 1 PIV data in Figure 7b. The lateral extent of the shock stems and their sweep toward the side wall are extracted from the Plane 2 PIV data in Figure 7c. The profiles are lofted between these anchor profiles and bounded by the sonic surface. The six shock structures are rendered in Figure 10 as red surfaces.

V. Isolator Approach Conditions

The models of interest each relate the monotonically increasing component of the shock train pressure profile to the quasi-1D approach conditions just upstream of the shock train. Defining these conditions is the last tool building step in this study before proceeding to evaluating the efficacy of the models and their assumptions from Table 1. The approach conditions relevant to the models of interest include the flux-conserved Mach number, M_1, momentum thickness Reynolds number, Re_θ, boundary layer confinement ratio or blockage ratio, $C_\theta = A_\theta/A$, and friction coefficient, C_f. The effect of each condition can be collapsed together into the Waltrup-Billig factor, Q, defined in Equation 8 [4, 7, 14].

$$Q = \left(M_1^2 - 1\right) \mathrm{Re}_\theta^{1/5} \left(\frac{A_\theta}{A}\right)^{-1/2}. \tag{8}$$

For each measurement type, the approach conditions are extracted at the shock foot location, s_f, from CFD of

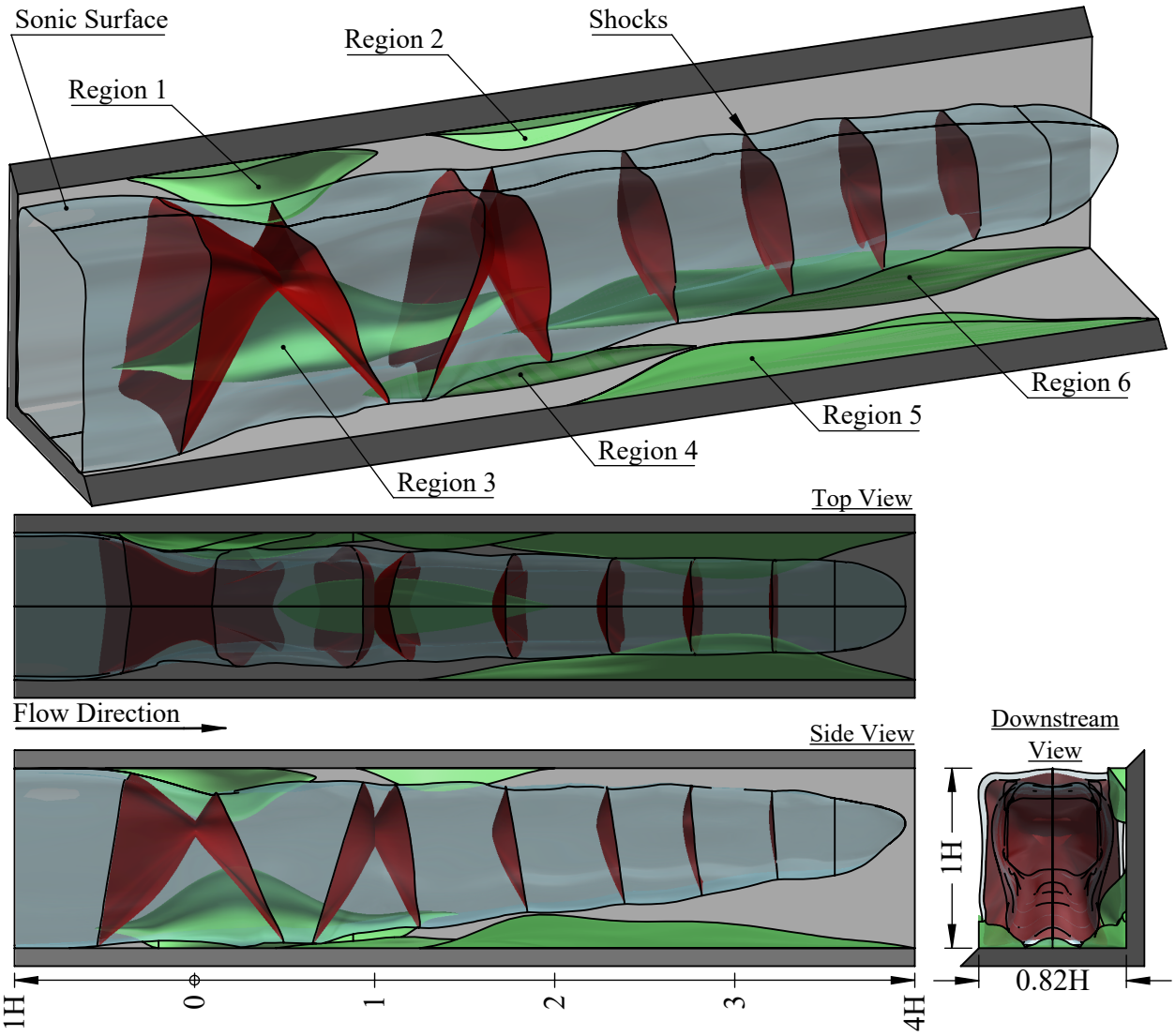

Fig. 10 Three-dimensional schematic of the shock train structure. Separated region laterally symmetric to Region 3 is removed for clarity.

the unbackpressured flow in the complete facility geometry. This approximates the first point at which the upstream influence of the shock train impacts the undisturbed approach conditions estimated by the CFD. The NASA Langley VULCAN Reynolds-averaged Navier-Stokes solver with a $k-\omega$ turbulence model, commonly applied to internal flows at NASA Langley [29], was used. A converged, wall-resolved structured grid is applied with 28 million cells and a y^+ range of 0.0003 to 0.3. The resulting mass flow error from the computation is minimal at 0.008%.

Differing experimental requirements for each measurement type necessitated different tunnel configurations, data acquisition systems, and optical configurations. The practical result of this is different streamwise shock train positions with different associated approach conditions for each measurement type. These are set by adjusting the downstream butterfly valve to target a specific isolator pressure ratio, P_B/P_A. Because of this necessity, the shock train approach

Table 2 Shock train approach conditions and scaling parameters for each dataset. This information was extracted from CFD at the streamwise location of the shock foot, s_f/H.

Data Type	s_1/H	M_1	Re_θ	Blockage Ratio, $\frac{A_\theta}{A}$	$Q = (M_1^2 - 1)Re_\theta^{1/5}\left(\frac{A_\theta}{A}\right)^{-1/2}$	P_B/P_A
Schlieren	6.34	1.88	6613	0.0339	80.6	3.20
Wall Pressure	7.07	1.86	7301	0.0375	75.3	3.10
Oil Flow	8.80	1.81	8944	0.0458	65.2	2.87
Streamwise PIV	6.89	1.87	7131	0.0366	76.5	3.13
Cross-Sectional PIV	7.22	1.86	7442	0.0383	74.3	3.08
Quasi-2D DNS [30]	N/A	1.72	7560	0.0323	63.8	N/A

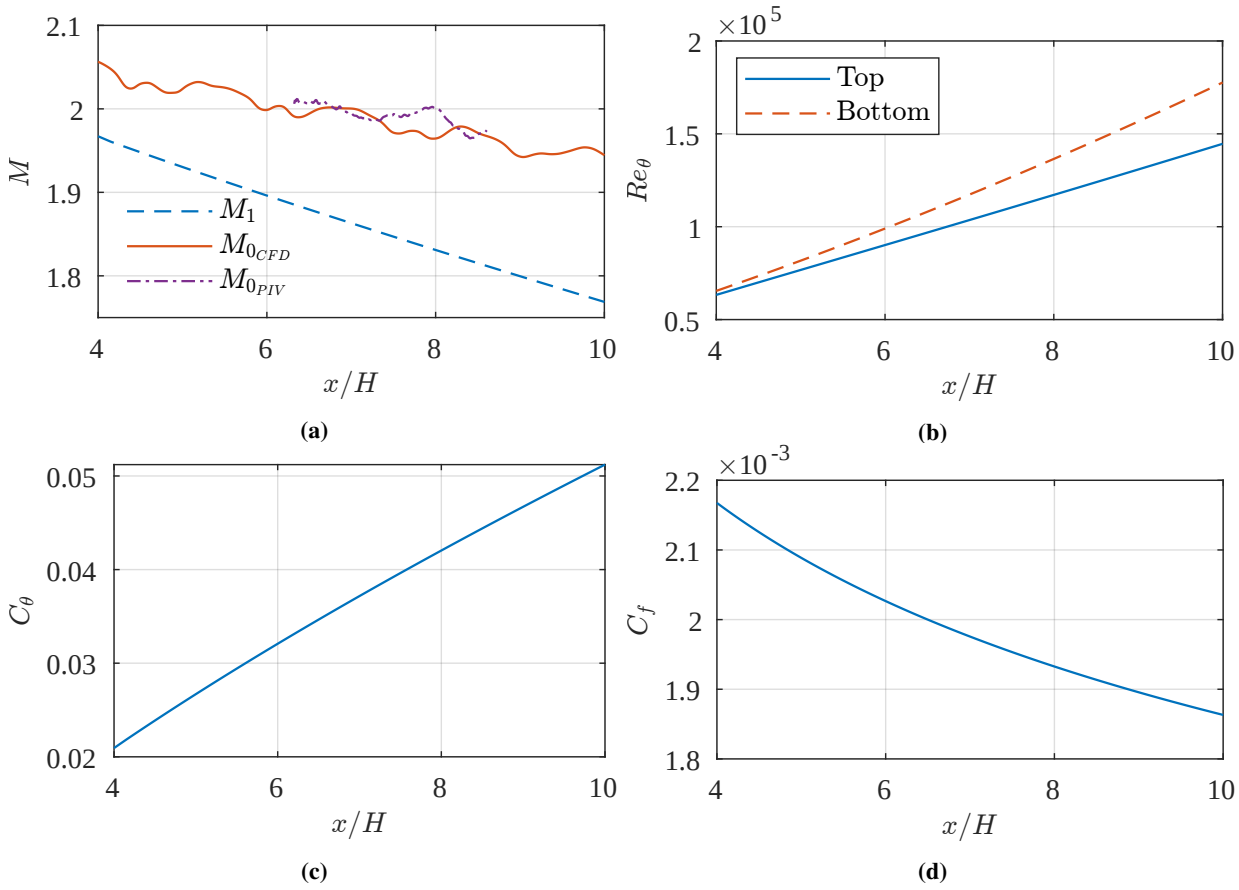

Fig. 11 Flow conditions of the unbackpressured facility (i.e., no shock train present) computed via CFD.

conditions for each measurement type differ as listed in Table 2. With the exception of the oil flow visualization, all Waltrup-Billig factors, Q, and tunnel positions are sufficiently close to analyze the time-averaged structure of the shock train based on the limited structural sensitivity to position previously observed in this operating range [12]. The difference in Q for the oil flow visualization relative to the other methods is acceptable to infer the qualitative structure of the boundary layer beneath the shock train.

The streamwise curves of the different approach conditions extracted from CFD are shown in Figure 11. Figure 11a shows that the modeled values for thrust-averaged Mach number agree well with the PIV measured values. The effect of the asymmetric facility nozzle is shown by the centerline Re_θ profiles in Figure 11b. The contoured top wall, in solid blue, is exposed to the local favorable pressure gradient of the nozzle curvature. The bottom wall, in dashed red, is flat through the subsonic and supersonic regions of the nozzle and is acted on by the more distributed reflection of the contoured expansion system. As a result, the bottom wall boundary layer is thicker than that on the top wall with a higher growth-rate. At $x/H = 7$, this results in a 20% difference in momentum thickness between the top and bottom walls. The importance of this boundary layer asymmetry relative to the overall structure of the flow is discussed later in further detail.

VI. Efficacy of Common Pseudoshock Models

With the necessary tools prepared, the literature models of interest are now compared to the available experimental data to assess their predictive capability and the validity of their underlying assumptions. First, suitable, quasi-1D reference curves for wall static pressure, P/P_1, thrust-averaged Mach number, M, and stream-tube area, $A_c/A = A_{\delta^*}/A$, are extracted from the available experimental datasets and shown as black curves with RMS uncertainty bands in Figure 12. Wall pressure scanner data yields the representative pressure profile in Figure 12a. The PIV data is extrapolated to the wall using a 1/7 power law profile and a linear interpolation is then applied between the two streamwise planes to create a profile representative of the full cross-section. This interpolation procedure is consistent with standard practice for shock trains [14, 19] and yields a reasonable approximation of the full cross-sectional velocity profile. Integration of these profiles at each streamwise grid point along the isolator yields reference Mach number and streamtube area curves in Figures 12b and 12c, respectively. The Waltrup-Billig correlation [14], Smart [15] flux-conserved model, and Fiévet et al. [17] flux-conserved models at the experimental approach conditions are overlaid on these figures.

First, the Waltrup-Billig correlation in Equation 7 is plotted as a solid blue curve in Figure 12a. The observed performance quickly departs from the facility data, overestimating the pressure rise across the isolator. This is because the aspect ratio and Mach number for the tested case in this work are lower than the datasets used to calibrate the correlation [13, 14]. The increased corner influence at low aspect ratios and the weaker shock at lower Mach numbers superimposes to smear and reduce the pressure growth-rate across a single SBLI [31], an effect that is amplified in the interconnected series of SBLIs that constitute the shock train structure. While the correlation provides insight into the most relevant approach conditions, its empirical nature makes it poorly suited to address variations in isolator geometry, approach flow morphology, and approach Mach numbers outside its calibration range. Furthermore, the correlation does not provide any insight into the fluid dynamics of the pseudoshock beyond the monotonic pressure rise profile. It is this limitation that makes the flux-conserved approach more attractive than simply recalibrating the correlation against a

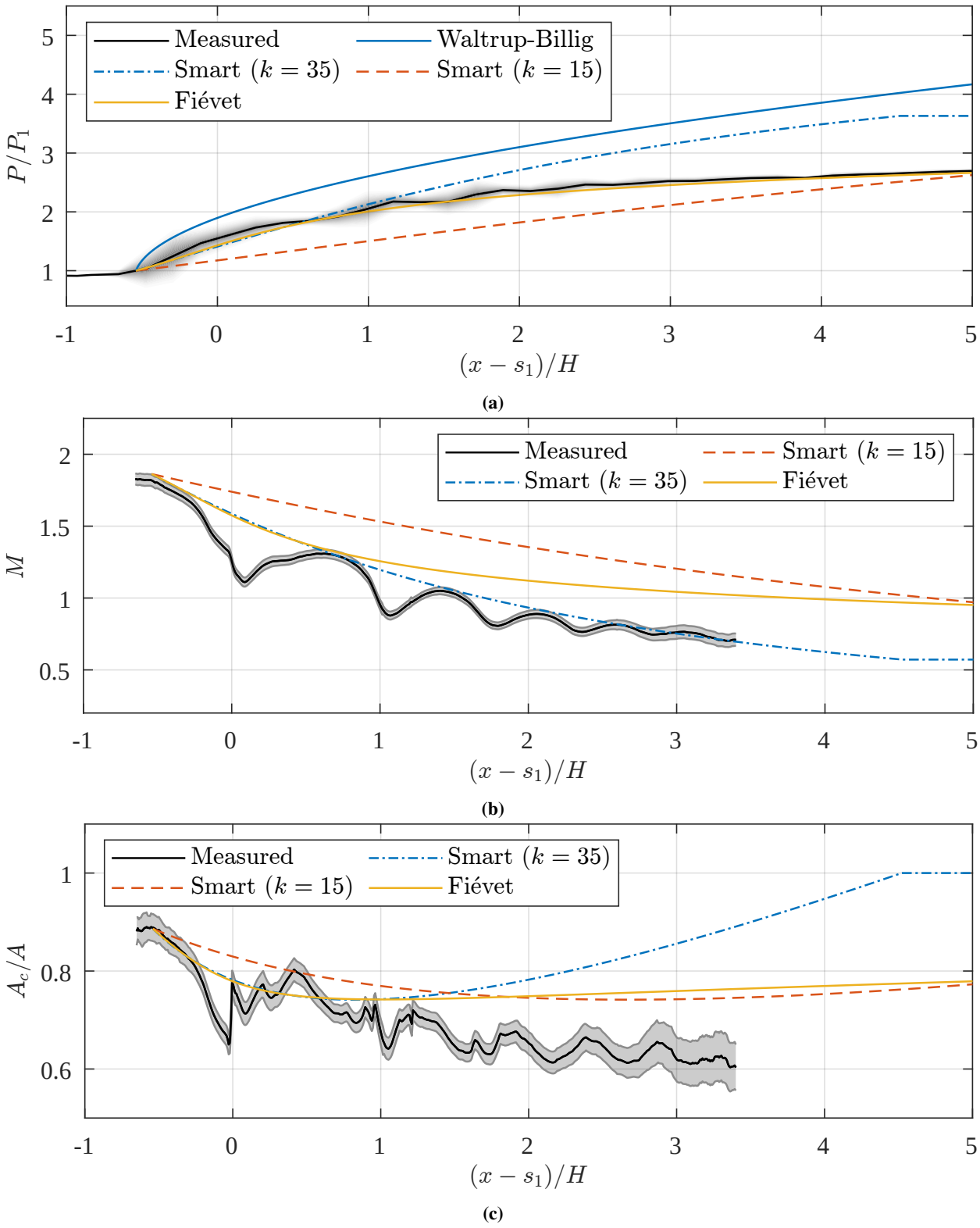

Fig. 12 Comparison of quasi-1D models against experimentally derived time-averaged values with RMS uncertainty bounds.

wider dataset.

The Smart [15] flux-conserved model is displayed in Figure 12 for kinetic energy conversion rate parameterizations $k = 35$ and $k = 15$ as blue dot-dashed and red dashed curves, respectively. The $k = 35$ parameterization best models the initial, high gradient region of the shock train while the $k = 15$ parameterization best models the pressure rise across the entire isolator. An engine designer using these curves to determine the appropriate isolator structure would underestimate the necessary structure with $k = 15$ and overestimate it using $k = 35$. While the overestimation of $k = 35$ would produce a safe engine, it also results in excess weight. Furthermore, implementing the closure model through the $\mathrm{d}P/\mathrm{d}x$ term in the system of equations imposes a mismatch between accurate prediction of the pressure profile and the flux-conserved fluid state, as set by M and A_c. This is best exemplified by the $k = 35$ case in Figure 12b, which produces a reasonable estimate of the Mach number profile while overpredicting the pressure downstream of the initial, high gradient region.

Fiévet et al. [17] observed this issue and proposed to replace the single parameter derivation of the Ortwerth model with a nine parameter model that allows the value of k to monotonically decrease as a power function of the local dynamic pressure, q. The nine model parameters are reoptimized using successive genetic algorithm minimization in this study against pressure profiles from the facility at isolator pressure ratios of 2.5-3.25. The result is shown by the solid yellow curves in Figure 12. The reoptimized Fiévet model is flexible such that it can perfectly model the pressure profile in Figure 12a. However, the Mach number and stream tube area predicted on Figures 12b-c diverge from the data after $x/H \approx 1$. Similar to the Smart model, this indicates missing flow physics that cannot be resolved through the Ortwerth pressure gradient closure model.

VII. Discussion of Model Deviations from Measurements

Given that the above comparison shows poor agreement between the prominent pseudoshock models in the literature and the facility data, further investigation is warranted.

A. Isolator Fluid Structures and Asymmetry

A distinctly asymmetric shock train structure is rendered by the available measurements into Figure 10. One might attribute this asymmetry solely to the asymmetric facility nozzle. However, schlieren imaging and CFD of Mach 2.5 shock trains in symmetric and asymmetric nozzle configurations at aspect ratios of 1.0, 3.0, and 6.0 by Geerts and Yu [32] show no distinct, vertical asymmetry in the shock train. While there are slight differentials between top, bottom, and side boundary layer momentum thicknesses at the approach conditions in their data, the degree of asymmetry does not grow between the start and end of the shock train [32]. Similarly, the facility nozzle in this study yields a momentum thickness difference between the flat bottom wall and the contoured upper wall of only 20% at the shock train leading edge, as shown in Figure 11b. In contrast, the asymmetry of the boundary layer thickness grows to a 200% vertical

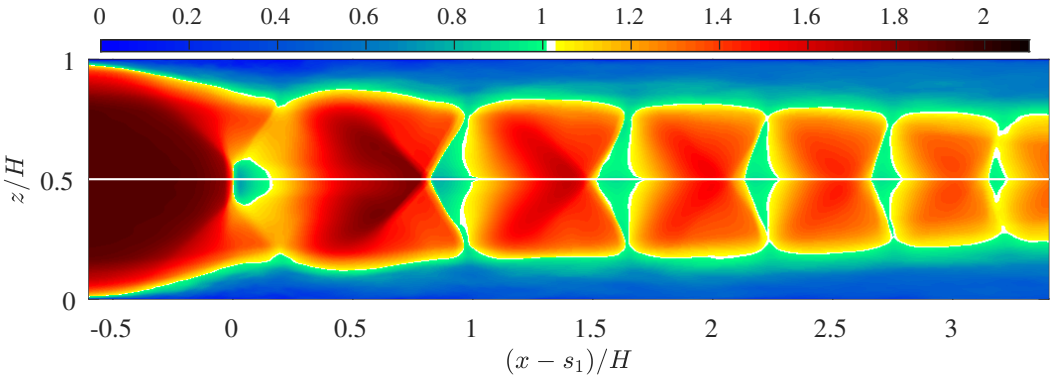

Fig. 13 Average Mach number contours from the symmetric DNS [30]. The dominant streamline through the strongest portion of each SBLI is marked as a white line.

asymmetry by the end of the shock train at $x/H = 4$ in Figure 7b. Based on this, we infer that there is another fluid dynamical structure or phenomenon at work in the facility to produce the substantial observed asymmetry.

Figure 8a shows the undisturbed corner flow $\overline{u}$ field just upstream of the shock train overlaid with streamlines of the in-plane flow. The dominant flow feature is a side wall vortex with a core at $z/H = 0.32$ extracting streamwise momentum from the side wall boundary layer at $0.1 \leq z/H \leq 0.25$. Previously observed by Morajkar et al. [33], this vortex appears to originate within or upstream of the facility nozzle, though its precise origin is beyond the scope of this study. The bottom of the vortex corresponds to a locally thickened side wall boundary layer in Figure 8a, preconditioned to separate at $z/H \approx 0.2$. This aligns with the origin of separated region 3 on the side wall and corresponds directly to the thickest point of separated flow in the cross-sectional SPIV Planes in Figures 8b-8f, as defined by the dashed 50% reversed flow line.

This upstream originating vortex is interpreted to be the driving force that skews the leading SBLI away from the corner bisector symmetry of a typical SBLI [33, 34]. Further reinforcing this inference is that the upper corner separation bubble, Region 1, where no additional side wall vortex is present, shows a traditional structure originating and closing in the corner. The size and intensity of Region 1 and 2 at the top wall is also markedly weaker than that of Regions 3-6 observed at the bottom wall. This indicates that the flow below the shock train core is deprived of more energy and momentum than the flow above the core. Based on these observations, it is theorized that the larger bottom corner separation bubble and its associated momentum losses skew the core flow at an upward angle, cascading the initial asymmetry induced by the side wall vortex into a substantially modified shock train structure.

The quantitative effect of the skewed shock train is observed by following a streamline passing through the strongest portion of each SBLI, marked as a dot-dashed line in Figure 7b. This is compared to direct numerical simulation (DNS) computations performed previously by Fiévet and Raman [30] and shown in Figure 13. Fiévet performed the DNS without a nozzle by initializing the turbulent boundary layer thickness and flow properties to match the facility isolator

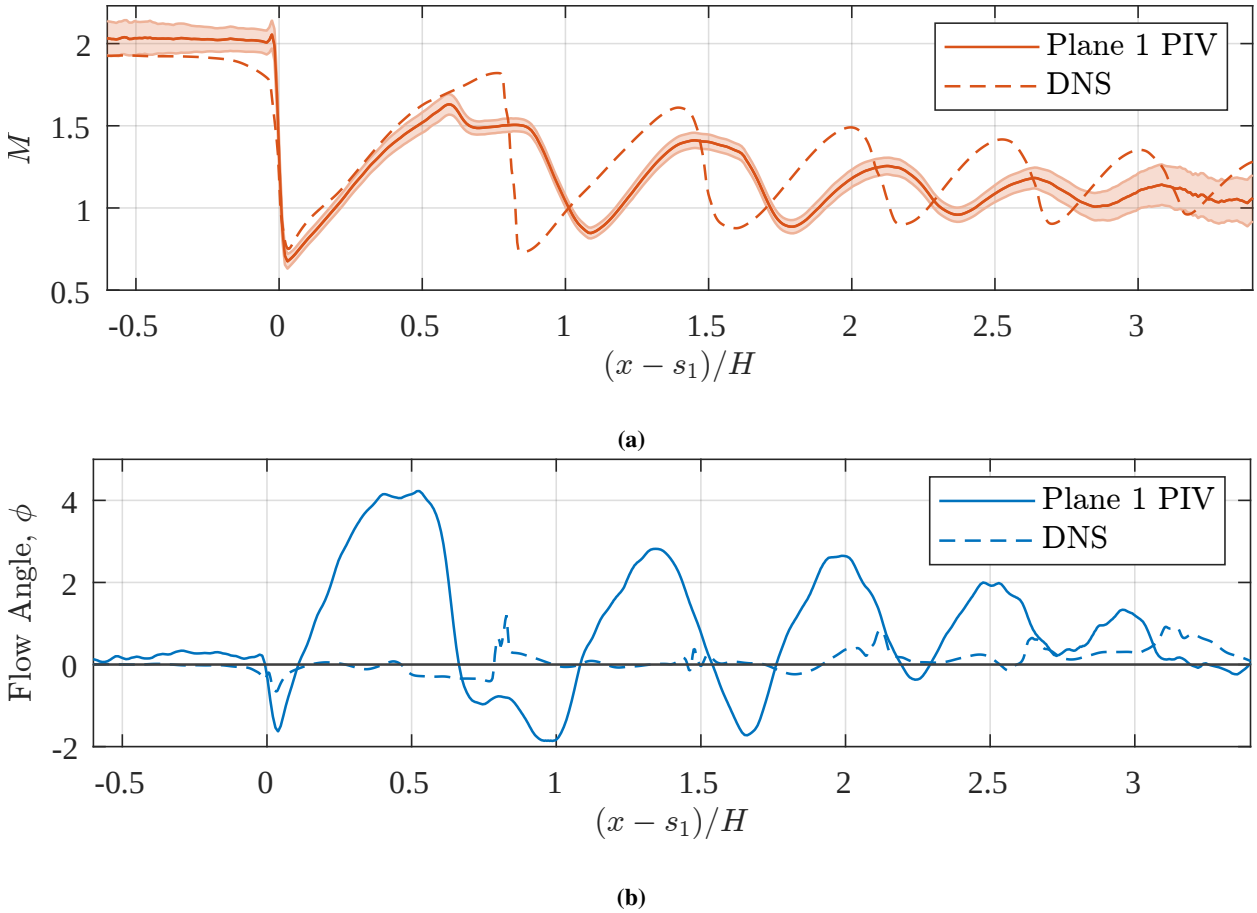

Fig. 14 Comparison of PIV data to DNS of (a) Mach number with RMS uncertainty bounds and (b) flow angle along the dominant streamline (white dashed line in Figure 7b) and Figure 13).

inflow. As such, it produces a symmetric shock train without the presence of a side wall vortex. The streamline Mach number, with RMS uncertainty bands, and the flow angle, ϕ, along the dominant streamlines for each case is compared in Figure 14. Significant upward flow turning is observed at each SBLI as the flow is confined by the separated flow. This effect is strongest for the first SBLI and weakens with each subsequent interaction.

The skew modifies the strength of each SBLI, which then modifies the compressive pressure recovery of the shock train. The effect of which is quantified by the dominant streamline Mach number profile in Figure 14a. The Mach number drops across the second through fifth SBLIs are 71%, 70%, 49%, and 35% of the equivalent symmetric DNS Mach number jump, respectively. The faster drop-off of SBLI compression in the skewed case fundamentally changes the balance between compressive mechanisms along the pseudoshock, and thus, the adverse pressure gradient that underlies the pressure profile output of the flux-conserved models.

The vortex induced skew has a significant impact on the underlying fluid dynamics of the shock train. This indicates that the assumptions of negligible transverse flow and momentum transfer, corresponding to items 2, 3, and 4 in Table 1 are invalid for this system. While the presence of the vortex is a characteristic of the nozzle, a similar vortex may form

within the inlet of an operational DMSJ engine. For example, at the mechanical joints between moving components of an adjustable inlet nozzle plate. As such, the impact of isolator flow morphology containing strong, near-wall vortices on the structure and response of the shock train must be assessed.

B. Separated Flow Morphology

Unlike in the modeled quasi-1D frame of Crocco and later Smart, flow separation in this study does not exist in a monolithic, interconnected region. But rather, it undergoes multiple reattachment and separation events at different areas in the cross-section as shown in Figure 10. Each separation bubble is supported by the alternating adverse and favorable pressure gradients within each shock cell. The result is that only $\sim 42\%$ of the wall surface area is exposed to separated flow. Thus, the remaining $\sim 56\%$ of the wall surface area in Figure 10 is not consistent with the assumption of $C_f = 0$. This implies the invalidity of assumptions 6 and 7 in Table 1 for the low aspect ratio case evaluated in this study.

The series of distinct separation bubbles drives the streamwise growth of the boundary layer confining the shock containing core. This creates a complex, interconnected relationship between the boundary layer morphology and the compression/re-expansion regions within each shock cell. Additionally, as the bubbles open and close, larger portions of the total mass flow is entrained into the boundary layer and away from the core, weakening the validity of assumption 9 in Table 1, that all the mass flow passes through the shock containing core.

The lack of a monolithic, separated boundary layer also limits the applicability of the Ortwerth pressure gradient closure model implemented in the Smart and Fiévet flux-conserved models. Ortwerth ties the adverse pressure gradient sustainable by the shock train to that sustainable by the boundary layer before separation. This inherently assumes that the boundary layer will separate completely under the influence of the shock train such that all compression is derived from a distributed conversion of kinetic to internal thermal energy within the shock containing core, as stated in assumption 11 in Table 1. However, the clear interplay between the morphology of the boundary layer and the strength of the shock system indicates this to be an inappropriately simplifying assumption for low aspect ratio and highly confined isolators.

VIII. Conclusions

Three quasi-1D pseudoshock models in the literature (the Waltrup-Billig correlation, the Smart flux-conserved model, and the Fiévet flux-conserved model) are evaluated to assess their efficacy in predicting the shock train state and pressure profile in a low aspect ratio isolator with an inflow Mach number of 2. The analysis indicates that the existing models, particularly the Fiévet flux-conserved model, can be calibrated well to wall pressure profiles in the isolator of interest. However, they all exhibit limited utility to an engine designer away from their calibrated conditions. A designer implementing the Waltrup-Billig correlation [13] will be limited to its tight, empirical calibration space. An implementation of the Smart flux-conserved model [15] can bound the problem of isolator length and structure, but it

lacks the flexibility to provide an estimate of how that structure must be distributed. Finally, with enough experimental or highly-resolved CFD data, the Fiévet flux-conserved model [17] can be calibrated to provide an excellent estimate of length and structure. However, this calibration data is expensive to obtain early in a design program, where such a model would be most applicable. Furthermore, the disconnect between the pressure profile and the underlying physical state of the system, such as the average Mach number, indicates that important flow physics relevant to the shock train measured in this study is missing from current model implementations.

To understand the divergence between the prevailing literature models and the low aspect ratio, highly confined shock train observed in this study, the model assumptions were assessed. To do this, schlieren imaging, particle image velocimetry, oil flow visualization, and wall pressure measurements are synthesized to render the three-dimensional normal bifurcated shock train structure. First, the quasi-1D assumptions were assessed by inspecting the undisturbed flow in the isolator. It was found that the presence of a side wall vortex extending downstream from the facility nozzle imposed strong asymmetry on the flow separation and overall shock train structure. The vortex extracts momentum from the side wall boundary layer, preconditioning it to separate before the corner. This is observed to shift the separation under the adverse pressure gradient of the shock train upward, skewing the structure of the shock boundary layer interactions. The separated flow morphology throughout the shock train is thus biased downward, growing the bottom wall boundary layer faster than that of the top wall boundary layer. This skews the angle of the supersonic core upward, adjusting the strength of each subsequent SBLI. In turn, the streamwise pressure gradient underlying the quasi-1D pressure profile is changed. While this vortex is an idiosyncrasy of the experiment, a similar vortex may form within a engine inlet creating a similar skew in an operational isolator. Furthermore, the separated flow morphology is found not to be monolithic, as is typically assumed, resulting in significant changes to the momentum balance in the system that drives the structure of the shock train and compression processes. The distortion resulting from these assumptions breaking down is not accounted for in the prevalent literature models.

The degree to which the underlying assumptions of the modern models breakdown for the low aspect ratio, Mach 2 isolator shock train observed in this study indicates an important gap in capability. This in turn limits the ability of engine designers to optimize isolator length and structure during the design phase of a DMSJ engine. Combined with the disconnect between the predicted pressure profile and the underlying fluid state of the shock train, this indicates the need for model modification and enhancement. Specifically, an extension of the underlying assumptions to better reflect the inherent, three-dimensional complexity of the DMSJ system.

Acknowledgments

Louis Edelman acknowledges the financial support of the Office of Naval Research through the National Defense Science and Engineering Graduate (NDSEG) Fellowship program and the continued support of the NASA Langley Research Center Flow Physics and Control, Hypersonic Airbreathing Propulsion, and Supersonic/Hypersonic Testing

branches.

References

[1] Matsuo, K., Miyazato, Y., and Kim, H.-D. D., "Shock Train and Pseudo-Shock Phenomena in Internal Gas Flows," *Progress in Aerospace Sciences*, Vol. 35, No. 1, 1999, pp. 33–100. doi:https://doi.org/10.1016/S0376-0421(98)00011-6.

[2] Gnani, F., Zare-Behtash, H., and Kontis, K., "Pseudo-Shock Waves and Their Interactions in High-Speed Intakes," *Progress in Aerospace Sciences*, Vol. 82, No. April, 2016, pp. 36–56. doi:https://doi.org/10.1016/j.paerosci.2016.02.001.

[3] Im, S. k., and Do, H., "Unstart Phenomena Induced by Flow Choking in Scramjet Inlet-Isolators," *Progress in Aerospace Sciences*, Vol. 97, 2018, pp. 1–21. doi:https://doi.org/10.1016/j.paerosci.2017.12.001.

[4] Hunt, R., Edelman, L. M., and Gamba, M., "Scaling of Pseudoshock Length and Pressure Rise," *2018 AIAA Aerospace Sciences Meeting*, American Institute of Aeronautics and Astronautics, Kissimmee, FL, 2018. doi:https://doi.org/10.2514/6.2018-1617, 2018-1617.

[5] Sugiyama, H., Takeda, H., Zhang, J., Okuda, K., and Yamagishi, H., "Locations and Oscillation Phenomena of Pseudo-Shock Waves in a Straight Rectangular Duct," *Japan Society of Mechanical Engineers International Journal Ser. 2, Fluids Engineering, Heat Transfer, Power, Combustion, Thermophysical Properties*, Vol. 31, No. 1, 1988, pp. 9–15. doi:https://doi.org/10.1299/jsmeb1988.31.1_9.

[6] Hunt, R. L., and Gamba, M., "On the Origin and Propagation of Perturbations that Cause Shock Train Inherent Unsteadiness," *Journal of Fluid Mechanics*, Vol. 861, 2019, pp. 815–859. doi:https://doi.org/10.1017/jfm.2018.927.

[7] Sullins, G. A., and McLafferty, G. H., "Experimental Results of Shock Trains in Rectangular Ducts," *4th Symposium on Multidisciplinary Analysis and Optimization*, American Institute of Aeronautics and Astronautics, Orlando, FL, 1992. doi:https://doi.org/10.2514/6.1992-5103, 1992-5103.

[8] Carroll, B. F., and Dutton, C. J., "Characteristics of Multiple Shock Wave/Turbulent Boundary Layer Interactions in Rectangular Ducts," *1st National Fluid Dynamics Conference*, American Institute of Aeronautics and Astronautics, Cincinnati, OH, 1988. doi:https://doi.org/10.2514/6.1988-3803, 1988-3803.

[9] Morgan, B., Duraisamy, K., and Lele, S. K., "Large-Eddy Simulations of a normal shock train in a constant-area isolator," *AIAA Journal*, Vol. 52, No. 3, 2014, pp. 539–558. doi:https://doi.org/10.2514/1.J052348.

[10] Fiévet, R., Koo, H., Raman, V., and Auslender, A. H., "Numerical Investigation of Shock-Train Response to Inflow Boundary-Layer Variations," *AIAA Journal*, Vol. 55, No. 9, 2017, pp. 2888–2901. doi:https://doi.org/10.2514/1.J055333.

[11] Geerts, J. S., and Yu, K. H., "Corner flow Separation From Shock Train/Turbulent Boundary-Layer Interactions in Rectangular Isolators," *20th AIAA International Space Planes and Hypersonic Systems and Technologies Conference, 2015*, American Institute of Aeronautics and Astronautics, Glasgow, Scotland, 2015. doi:https://doi.org/10.2514/6.2015-3546, 2015-3546.

[12] Hunt, R. L., and Gamba, M., "Shock Train Unsteadiness Characteristics, Oblique-to-Normal Transition, and Three-Dimensional Leading Shock Structure," *AIAA Journal*, Vol. 56, No. 4, 2018, pp. 1569–1587. doi:https://doi.org/10.2514/1.J056344.

[13] Waltrup, P. J., and Billig, F. S., "Structure of Shock Waves in Cylindrical Ducts," *AIAA Journal*, Vol. 11, No. 10, 1973, pp. 1404–1408. doi:https://doi.org/10.2514/3.50600.

[14] Billig, F. S., "Research on Supersonic Combustion," *Journal of Propulsion and Power*, Vol. 9, No. 4, 1993, pp. 499–514. doi:https://doi.org/10.2514/3.23652.

[15] Smart, M. K., "Flow Modeling of Pseudoshocks in Backpressured Ducts," *AIAA Journal*, Vol. 53, No. 12, 2015, pp. 3577–3588. doi:https://doi.org/10.2514/1.J054021.

[16] Vanstone, L., Lingren, J., and Clemens, N. T., "Simple Physics-Based Model for the Prediction of Shock-Train Location," *Journal of Propulsion and Power*, Vol. 34, No. 6, 2018, pp. 1428–1441. doi:https://doi.org/10.2514/1.B37031.

[17] Fiévet, R., Raman, V., and Auslender, A. H., "Data-Driven One-Dimensional Modeling of Pseudoshocks," *Journal of Propulsion and Power*, Vol. 35, No. 2, 2019, pp. 313–327. doi:https://doi.org/10.2514/1.B37175.

[18] Edelman, L. M., and Gamba, M., "Rigid Body Response of a Mach 2 Shock Train to Downstream Forcing," *2018 Fluid Dynamics Conference*, American Institute of Aeronautics and Astronautics, Atlanta, GA, 2018. doi:https://doi.org/10.2514/6.2018-3542, 2018-3542.

[19] McLafferty, G., "Theoretical Pressure Recovery Through a Normal Shock in a Duct with Initial Boundary Layer," *Journal of the Aeronautical Sciences*, Vol. 20, No. 3, 1953, pp. 169–174. doi:https://doi.org/10.2514/8.2582.

[20] Torizumi, Y., "One-Dimensional Treatment of Compressible Flow through a Duct," *Transactions of the Japan Society of Mechanical Engineers Series B*, Vol. 58, No. 549, 1992, pp. 1650–1653. doi:https://doi.org/10.1299/kikaib.58.1650.

[21] Matsuo, K., Miyazato, Y., and Kim, H. D., "Mass-Averaging Pseudo-Shock Model in a Straight Flow Passage," *Proceedings of the Institution of Mechanical Engineers: Journal of Aerospace Engineering, Part G*, Vol. 213, No. 6, 1999, p. 365. doi:https://doi.org/10.1243/0954410991533089.

[22] Crocco, L., "One-Dimensional Treatment of Steady Gas Dynamics," *Fundamentals of Gas Dynamics: High Speed Aerodynamics and Jet Propulsion*, Princeton Legacy Library, Vol. 3, edited by H. W. Emmons, Princeton University Press, Princeton, NJ, 1958, 1st ed., pp. 64–349.

[23] Ortwerth, P. J., "Scramjet Flowpath Integration," *Scramjet Propulsion*, edited by S. Murthy and E. Curran, No. 189 in Progress in Astronautics and Aeronautics, American Institute of Aeronautics and Astronautics, Reston, VA, 2000, 1st ed., pp. 1105–1293.

[24] Samimy, M., and Lele, S. K., "Motion of Particles with Inertia in a Compressible Free Shear Layer," *Physics of Fluids A: Fluid Dynamics*, Vol. 3, No. 8, 1991, pp. 1915–1923. doi:https://doi.org/10.1063/1.857921.

[25] Shapiro, A. H., *Dynamic and Thermodynamics of Compressible Flow*, 1st ed., Vol. 1, Ronald Press Company, New York, NY, 1953.

[26] Wieneke, B., "PIV Uncertainty Quantification from Correlation Statistics," *Measurement Science and Technology*, Vol. 26, No. 7, 2015, p. 074002. doi:https://doi.org/10.1088/0957-0233/26/7/074002.

[27] Sciacchitano, A., Neal, D. R., Smith, B. L., Warner, S. O., Vlachos, P. P., Wieneke, B., and Scarano, F., "Collaborative Framework for PIV Uncertainty Quantification: Comparative Assessment of Methods," *Measurement Science and Technology*, Vol. 26, No. 7, 2015, p. 74004. doi:https://doi.org/10.1088/0957-0233/26/7/074004.

[28] Sciacchitano, A., and Wieneke, B., "PIV Uncertainty Propagation," *Measurement Science and Technology*, Vol. 27, No. 8, 2016, p. 084006. doi:https://doi.org/10.1088/0957-0233/27/8/084006.

[29] Di Stefano, M. A., Hosder, S., and Baurle, R. A., "Effect of Turbulence Model Uncertainty on Scramjet Isolator Flowfield Analysis," *Journal of Propulsion and Power*, Vol. 36, No. 1, 2020, pp. 109–122. doi:https://doi.org/10.2514/1.B37597.

[30] Fiévet, R., and Raman, V., "Effect of Vibrational Nonequilibrium on Isolator Shock Structure," *Journal of Propulsion and Power*, Vol. 34, No. 5, 2018, pp. 1334–1344. doi:https://doi.org/10.2514/1.B37108.

[31] Burton, D. M., and Babinsky, H., "Corner Separation Effects for Normal Shock Wave/Turbulent Boundary Layer Interactions in Rectangular Channels," *Journal of Fluid Mechanics*, Vol. 707, 2012, pp. 287–306. doi:https://doi.org/10.1017/jfm.2012.279.

[32] Geerts, J. S., and Yu, K. H., "Three-Dimensional Nature of Shock Trains in Rectangular Scramjet Isolators," *54th AIAA Aerospace Sciences Meeting*, American Institute of Aeronautics and Astronautics, San Diego, CA, 2016. doi:https://doi.org/10.2514/6.2016-1164, 2016-1164.

[33] Morajkar, R. R., Klomparens, R. L., Eagle, W. E., Driscoll, J. F., Gamba, M., and Benek, J. A., "Relationship Between Intermittent Separation and Vortex Structure in a Three-Dimensional Shock/Boundary-Layer Interaction," *AIAA Journal*, Vol. 54, No. 6, 2016, pp. 1862–1880. doi:https://doi.org/10.2514/1.J053905.

[34] Babinsky, H., and Harvey, J. K., *Shock wave-boundary-layer interactions*, 1st ed., Cambridge University Press, Cambridge ; New York, 2011. doi:10.1017/CBO9780511842757, publication Title: Shock Wave-Boundary-Layer Interactions.